

Hydrodynamic Shock Wave Studies within a Kinetic Monte Carlo Approach

Irina Sagert¹, Dirk Colbry², Terrance Strother³, Rodney Pickett², Wolfgang Bauer^{1,2}

¹*Department of Physics and Astronomy, Michigan State University, East Lansing, Michigan, 48824, USA*

²*Institute for Cyber-Enabled Research, Michigan State University East Lansing, Michigan 48824, USA*

³*XTD-6, Los Alamos National Laboratory, Los Alamos, New Mexico 87545, USA*

(Dated: October 31, 2012)

Kinetic approaches are routinely employed to simulate the dynamics of systems that are too rarified to be described by the Navier-Stokes equations. However, generally they are far too computationally expensive to be applied for systems that are governed by continuum hydrodynamics. In this paper, we introduce a massively parallelized test-particle based kinetic Monte Carlo code that is capable of modeling the phase space evolution of an arbitrarily sized system that is free to move in and out of the continuum limit. Using particle mean free paths which are small with respect to the characteristic length scale of the simulated system, we retrieve continuum behavior, while non-equilibrium effects are observed when the mean free path is increased. To demonstrate the ability of our code to reproduce hydrodynamic solutions, we apply a test-suite of classic hydrodynamic shock problems. Simulations using tens of millions of test-particles are found to reproduce the analytical solutions well.

PACS numbers: 47.45.Ab, 45.50.-j, 47.85.Dh, *43.25.Cb, 07.05.Tp, 82.20.Wt

I. INTRODUCTION AND MOTIVATION

In fluid dynamics, when the characteristic length scale of a flow does not greatly exceed the mean free path of the particles it is comprised of, the continuum approximation assumed by the Navier-Stokes (NS) equations breaks down and the particle nature of matter must be explicitly taken into account [1]. Under these conditions, flows are said to be rarified. The rarefaction of a flow is characterized by the Knudsen number Kn , which is defined as the ratio of the mean free path λ to a characteristic length scale of the system L :

$$Kn = \lambda/L. \quad (1)$$

While the continuum limit of hydrodynamics is applicable when $Kn \ll 1$, it is generally accepted that flows with $Kn > 0.01$ are not well described by the NS equations as they do not form a closed set in this regime [1]. There are currently many areas of research in which flows with large Knudsen numbers are relevant. The studies of hypersonic flow [2] and shock structure [1], simulation studies of space flight [3], nano-scale devices [4], particle production in heavy ion collisions [5–7], the dynamics of inertial confinement fusion (ICF) capsules [8–10], as well as out-of-equilibrium neutrino-matter interactions in core-collapse supernovae [11] all require the ability to model flows with $Kn > 0.01$. The latter two subjects are of particular interest to us.

Despite the enormous efforts poured into achieving thermonuclear ignition of ICF capsules at the National Ignition Facility (NIF), satisfactory yield has never been obtained. The ICF capsule experiments at NIF are guided by complex numerical simulations. All of the codes that suggest that the techniques employed thus far to ignite the nuclear fuel should have been successful use continuum hydrodynamics to describe the entire capsule system. The so-called “hot spot” of a typical ICF capsule, where thermonuclear burn is expected to initiate and shock fronts must be resolved, is approximately 25 micrometers across and has a density and temperature on the order of 100 g/cc and 10 keV respectively [12]. It is a trivial exercise to demonstrate that in this environment, the mean free path of a thermal deuteron, a critical component of the nuclear fuel, is on the order of a few micrometers. Clearly the continuum approximation is not applicable here. Furthermore, investigations of shock front kinetic effects depleting the ion distribution of fast particles in ICF capsules [8–10, 13–16] found that the resultant highly non-Maxwellian ion distributions may alter the hydrodynamics and thermonuclear yield of the capsules. Other studies suggest that capsule yield can also be diminished by kinetic effects associated with strong self-generated electric fields which can broaden the shock fronts [17, 18]. Consequently, there is a strong motivation to develop a kinetic model capable of fully resolving shock fronts in all regions of ICF capsules.

Many theories have been suggested to explain the core-collapse supernova explosion mechanism [19–24]. The determination of the role that neutrino-matter interactions play in the generation of these explosions remains an outstanding problem in physics (see e.g. [25] and references therein). Currently, the most commonly accepted model for core-collapse supernova explosions is based on deposition of energy by neutrinos that are produced in the central high temperature and density region of the collapsed stellar core into cooler less dense regions of the infalling matter [19, 20]. The simulations suggest that this so-called neutrino heating can power fluid instabilities that grow to large amplitudes and eventually power an explosion [26, 27]. To study such a scenario, an accurate description of the

supernova hydrodynamics as well as modeling neutrino transport in three dimensions seems to be ultimately required [28–31]. For one-dimensional simulations, it is possible to solve the full Boltzmann equations for neutrino propagation [32–34]. However, in two or three dimensions, this approach becomes computationally too expensive and approximations have to be made [35–39]. Monte Carlo neutrino transport has been suggested as an alternative approach since it is expected to scale better for multi-dimensional simulations (see [40] and references therein). This is one motivation for us to develop a large scale Monte Carlo transport code which can be used in supernova studies. Furthermore, most simulations operate with nuclear equations of state which evolve only one representative heavy nucleus instead of a full statistical ensemble of present nuclei. The inclusion of the latter could alter weak interaction processes and thereby the efficiency of neutrino heating as well as impact supernova nucleosynthesis [25, 41–43]. It has been demonstrated in previous works that a kinetic approach has the capability to treat baryon and neutrino dynamics identically and thereby evolve a full ensemble of nuclei and readily model out-of-equilibrium neutrino-matter interactions [11, 44]. Preliminary studies conducted with such an approach found that out-of-equilibrium neutrino-matter interactions with nuclei close to the neutron drip line could significantly impact the dynamics of the core-collapse and subsequent explosion [11, 44]. More detailed calculations are necessary to confirm the observed effects.

It is the long-term goal of this work to contribute to the modeling of systems which are influenced by out-of-equilibrium phenomena, such as ICF capsules and core-collapse supernovae. However, for realistic simulations, it is necessary to develop an approach capable of resolving macroscopic three-dimensional hydrodynamic shock fronts and describing non-continuum flows. The latter requirement necessitates abandoning the NS equations and adopting a kinetic description.

II. THE BOLTZMANN EQUATION

For non-continuum flows, the governing equation is the Boltzmann equation of kinetic theory. It is a nonlinear integro-differential equation that describes the time evolution of the statistical distributions of particles in a fluid that undergo binary collisions. The Boltzmann equation is valid for all Knudsen numbers and, in the limit of small mean free paths, leads to the continuum description [45]. For a fluid comprised of N different species of particles, the equation satisfied by the probability distribution function (PDF) of the i th species is [46]:

$$\frac{\partial f_i(\vec{r}, \vec{p}, t)}{\partial t} + \frac{\vec{p}}{m} \cdot \nabla f_i(\vec{r}, \vec{p}, t) + \vec{F} \cdot \frac{\partial f_i(\vec{r}, \vec{p}, t)}{\partial \vec{p}} = I_{i,\text{coll}}, \quad (2)$$

where \vec{r} , \vec{p} , and m_i are the position, momentum, and mass of particle i respectively, \vec{F} is the external force field, $f_i(\vec{r}, \vec{p}, t)$ is the number of particles of species i found in a differential phase space neighborhood of \vec{r} and \vec{p} at time t , and $I_{i,\text{coll}}$ is the term that takes into account the changes in f_i induced by two-body collisions. $I_{i,\text{coll}}$ is generally a sum of integrals involving the pre-collision and post-collision PDFs of all species present [46]. It is this collision term that couples the N equations and generally makes them very difficult to solve.

A. Analytic Solution techniques

While the Boltzmann equation is not generally solvable by analytical techniques, approximations can be employed to derive less complex equations. By making assumptions about the form of the PDFs, the Boltzmann equation can be used to derive approximate fluid dynamics equations of higher order in Knudsen number than the NS equations [2]. These higher-order fluid dynamic models are the so-called extended or generalized hydrodynamics equations. Another common approximate technique is to modify the Boltzmann equation itself. The most famous example of this is the Bhatnagar-Gross-Krook (BGK) [47] equation that replaces the collision term in eq.(2) with a relaxation term:

$$I_{i,\text{coll}} \rightarrow \frac{f_{M,i} - f_i}{\tau} \quad (3)$$

where $f_{M,i}$ is the Maxwell distribution for the i th species, f_i is the PDF of the i th species, and τ is a particle collision time. Despite the fact that the BGK equations are less complicated than the full Boltzmann equation, numerical techniques such as the lattice Boltzmann method or discrete velocity method [47–50] are typically required to solve them.

B. Numerical Simulation Techniques

In the absence of a general analytic solution technique for the full Boltzmann equation, simulation schemes that attempt to directly model the dynamics of a fluid using a large number of simulated particles have been developed. While it is possible to infer the PDFs from the simulated particles phase space coordinates, the problem can be formulated without reference to them. The first of these direct simulation approaches was the molecular dynamics (MD) method [51]. In these calculations, each physical particle is represented by a simulated particle. Many advances have been made in MD calculations providing unique insight to fluid dynamics on molecular scales [52–54]. However, the one-to-one physical-to-simulated particle ratio computationally limits MD calculations to volumes much smaller than many hydrodynamic features of interest.

C. The Test-Particle Method

In order to model the phase space evolution of systems that contain too many physical particles to make use of a MD-like direct simulation scheme, so-called test-particle methods are employed. These allow the physical-to-simulated particle ratio to greatly exceed one and thereby permit the modeling of macroscopic samples of fluids. Rather than attempting to discretize the entire phase space relevant to the simulated system and track the value of the phase space densities in each cell in time, the test-particle method only tracks the initially occupied phase space cells and represents them by imaginary test-particles. These are propagated in a way that models the physical evolution of the phase space. The test-particles interact with one another via one-body mean field forces and scatter with realistic cross sections.

Formally, the test-particle method approximates the phase space density with a sum over delta functions [55]

$$f(\vec{r}, \vec{p}, t) = \sum_{i=0}^{N_{\text{tp}}} \delta^3(\vec{r} - \vec{r}_i(t)) \delta^3(\vec{p} - \vec{p}_i(t)), \quad (4)$$

where N_{tp} is the total number of test-particles. The initial coordinates of these delta function test-particles are determined by the initial conditions of the simulated system. Inserting this solution into the system transport equations such as the Boltzmann equations in eq.(2) generates the following set of simple first-order linear differential equations that govern the motion of the i^{th} test-particle's centroid coordinates in the full six-dimensional phase space:

$$\begin{aligned} \frac{d}{dt} \vec{p}_i &= \vec{F}(\vec{r}_i) + \vec{C}(\vec{p}_i) \\ \frac{d}{dt} \vec{r}_i &= \frac{\vec{p}_i}{m_i} \\ i &= 1, \dots, N_{\text{tp}}. \end{aligned} \quad (5)$$

Here $\vec{F}(\vec{r}_i)$ is the mean field one-body force acting on the i^{th} test-particle, and $\vec{C}(\vec{p}_i)$ symbolizes the effects that two-body collisions with other test-particles have on the i^{th} test-particle's momentum.

For a system comprised of N_{phys} physical particles being modeled with N_{tp} test-particles, the ratio $N_{\text{phys}}/N_{\text{tp}}$ effectively determines a cutoff scale below which details cannot be resolved. Naturally, the test-particle approach is applicable as long as N_{tp} is sufficiently large to capture the gross dynamics of the system's phase space. When $N_{\text{phys}}/N_{\text{tp}}$ becomes too large, some "small-scale" phenomena can become impossible to resolve. It must therefore be established that these details do not impact the gross phase space dynamics and/or can be taken into account indirectly. The former can be accomplished with convergence tests.

However, multiscale problems are certainly not unique to the test-particle approach. Hydrodynamic calculations have to spatially discretize simulated systems. When the corresponding volumes are too large the same scale and resolution concerns can occur. Representative particle models, which are very similar to test-particle calculations in the large $N_{\text{phys}}/N_{\text{tp}}$ limit, have to contend with scale and resolution issues as well when the importance sampling of the particles the system is comprised of is made. Failure to represent physical particles with certain characteristics with a sufficient number of representative particles can prevent calculations from resolving details that are essential to the gross system behavior.

III. THE DSMC TECHNIQUE

The test-particle method employs probabilistic procedures to model two-body collisions. It is therefore classified as a Direct Simulation Monte Carlo (DSMC) technique [14, 56, 57]. The primary approximation of the DSMC approach

is the decoupling of the motion and the collisions of simulated particles during sufficiently small time intervals. DSMC techniques employ an operator splitting method to separate the Boltzmann equation into two processes: transport and collisions. Simulated particle motions are calculated deterministically and two-body collisions between them are modeled probabilistically. Though variations exist between different implementations of DSMC algorithms, a given iteration can be described by four basic processes: sample flow field, move the particles accordingly, organize the particles into a scattering grid, and model two-body collisions. The first two processes involve evaluating the flow field forces acting on the simulated particles and then solving the resultant first-order linear differential equations of motion. The third process consists of dividing the simulated volume into grid cells and organizing the particles into them. The size chosen for the scattering grid cells can depend strongly upon the way the two-body collisions are modeled in the forth step of the iteration.

A common approach to implement two-body particle scattering is to model collisions only between particles in the same scattering grid cell wherein the collision partners are selected randomly [14, 58, 59]. It has been demonstrated that, in the limits of infinite simulated particle count and vanishing scattering grid cell and time step sizes, DSMC algorithms that employ this type of scattering technique yield results that converge to known solutions of the Boltzmann equation [60]. In particular, this scattering technique has been used extensively and with great success in the simulation of microscopic flows [58, 61–63].

To avoid unphysical collisions between simulated particles that are too far apart from each other in a given time step, the size of the scattering grid cells has to be tightly connected to mean free path of the physical particles. This requirement can make scattering algorithms of this type prohibitively expensive for flows with mean free paths and particle collision times much smaller than the characteristic scales for lengths and times. For such flows, a way of modeling two-body collisions that selects scattering pairs more judiciously is required.

In this work we apply such an altered DSMC algorithm for the detection and performance of particle collisions. Our approach will be described in sections IV and V, while in section VI we present our results for shock wave modeling with the kinetic approach. The paper is closed with the conclusions and outlook in sections VIII and IX, respectively.

IV. THE DISTANCE-OF-CLOSEST-APPROACH METHOD FOR SCATTERING PARTNER SEARCH

Unlike in traditional DSMC algorithms where scattering partners are chosen randomly from a grid cell, in our approach the possible collision between two test-particles is determined from their distance of closest approach d_{\min} . If the latter is reached during a timestep Δt the paths of two particles A and B can cross and a collision is possible. To detect an intersection of particle paths, the relative position vectors \vec{r}_{rel} at the current as well as the next timestep:

$$\vec{r}_{\text{rel}}(t) = \vec{r}_A(t) - \vec{r}_B(t), \quad \vec{r}_{\text{rel}}(t + \Delta t) = \vec{r}_A(t + \Delta t) - \vec{r}_B(t + \Delta t) \quad (6)$$

have to be projected on the corresponding relative velocity vectors \vec{v}_{rel} . This results in the crossing number:

$$\chi = (\vec{r}_{\text{rel}}(t) \cdot \vec{v}_{\text{rel}}(t))(\vec{r}_{\text{rel}}(t + \Delta t) \cdot \vec{v}_{\text{rel}}(t + \Delta t)). \quad (7)$$

A negative value of χ indicates that within the time step Δt , the particles have reached d_{\min} and their paths have crossed. This is a first indication of a possible collision. However, its occurrence depends on the interaction cross-section σ , i.e. the particle mean free path λ . Both can be related to an effective particle interaction radius r_{eff} via:

$$\lambda = (\sigma n)^{-1} = (4\pi r_{\text{eff}}^2 n)^{-1}, \quad (8)$$

whereas $n = N/V$ is the number of particles N per volume V . Two possible scattering partners A and B can only interact with each other if their distance of closest approach is within the sum of the effective radii $d_{\min} \leq (r_{\text{eff},A} + r_{\text{eff},B})$. The collision time t_c can then be calculated from:

$$|\vec{r}_{\text{rel}} + \vec{v}_{\text{rel}} t_c| = r_{\text{eff},A} + r_{\text{eff},B}, \quad (9)$$

$$|\vec{v}_{\text{rel}}|^2 t_c^2 + 2(\vec{v}_{\text{rel}} \cdot \vec{r}_{\text{rel}}) t_c + |\vec{r}_{\text{rel}}|^2 = (r_{\text{eff},A} + r_{\text{eff},B})^2 \quad (10)$$

to:

$$t_{c,1,2} = \frac{1}{|\vec{v}_{\text{rel}}|^2} \left[-(\vec{v}_{\text{rel}} \cdot \vec{r}_{\text{rel}})^2 \pm \sqrt{(\vec{v}_{\text{rel}} \cdot \vec{r}_{\text{rel}})^2 - |\vec{v}_{\text{rel}}|^2 (|\vec{r}_{\text{rel}}|^2 - (r_{\text{eff},A} + r_{\text{eff},B})^2)} \right]. \quad (11)$$

If the collision times $t_{c,1}$ and $t_{c,2}$ are real numbers a collision can take place. In case the particle distance is larger than the sum of the effective radii, that is $|\vec{r}_{\text{rel}}| \gg (r_{\text{eff},A} + r_{\text{eff},B})$, the particle cross-sections are too small and the collision

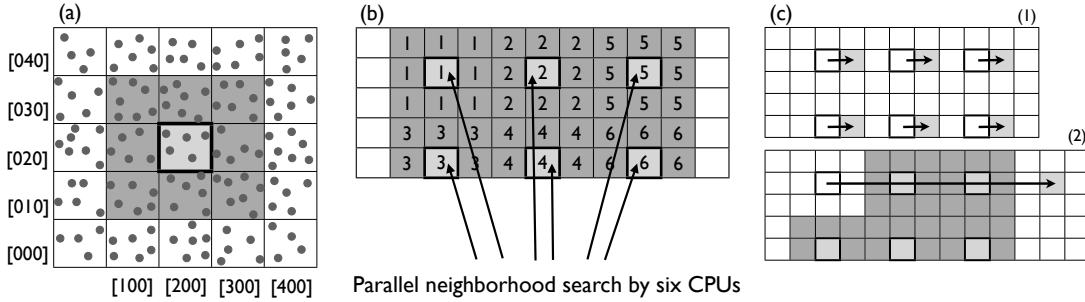


FIG. 1: (a) Visualization of a 2D particle setup with 25 bins. The active bin is located at the center (light grey), surrounded by its 8 neighborhood bins (dark grey). (b) Parallel neighborhood binary collision detection performed by six processors in the active bins. The neighboring bins are numbered according to their active bins. (c) Two possibilities for the progress of a parallel scattering partner search for six CPUs. (1) Simultaneous update of active bins for all CPUs. (2) Individual CPU update of the active bin. The latter can not be part of the neighborhood in the ongoing collision detection of the remaining 5 processors.

times are imaginary. Negative values of $t_{c1,2}$, on the other hand, indicate that the effective radii of particles A and B are overlapping already at the current time step. This situation can occur frequently for high particle densities or if the value of λ is chosen much smaller than the distance a test-particle can travel within Δt . As will be described in the next section, we distinguish between positive and negative collision times by choosing a slightly different approach for position update of the corresponding particles.

Typically, the analysis of t_c finds several potential collision partners for each particle. Once the latter have been determined, the final partners can be chosen either according to the shortest collision time or the smallest distance between scattering partners. In general, the potential impact that the screening of scattering partners by other test-particles has on physical scattering cross sections must be taken into account (see e.g. [64] and references therein). However, these effects can be avoided by requiring that the scattering partner selected for a given test-particle is always the closest of the potential candidates. While it is true that for matter in the hydrodynamic limit, the scattering cross section is very large and therefore the impact of screening might be negligible, we also find in our approach that the scattering partner determination according to the shortest distance proves itself as most suitable. We will discuss this in more detail in the next section.

V. SIMULATION SETUP

A main motivation of our work is to set up an algorithm for collision detection which is efficient and scales well to large simulations. The most computationally expensive step is the determination of scattering partners. A brute force approach would compare every particle to every other particle in the simulation. This is an $O(N^2)$ algorithm which could in theory run on P processors for an $O(N^2/P)$ running time. An alternative is to assume that scattering partners are found based on nearest neighbors search. A simple approach to nearest neighbor is to use a sorting algorithm which is $O(N \log N)$. Although there are methods for parallel sorting, this is still an expensive alternative and will not scale well to larger systems. For this work we choose to find scattering partners using spatial binning. Particles are placed into bins and then scattering partners are only searched for inside of a particular bin. The binning component of the algorithm takes linear time and will also scale linearly $O(N/P)$. The search for scattering partners is now determined by looking only at other particles in the same bin or close neighbors. If the maximum number of particles in a bin (N_{bin}) is much smaller than the total particles ($N_{\text{bin}} < \log N < N$) then this should significantly increase the computation time of the algorithm. Furthermore, this approach scales linearly for a total running time of $O(NN_{\text{bin}}^2/P)$.

For this work the determination of scattering partners was parallelized using shared memory parallelization (OpenMP). As is sketched in Fig.1 (a) and (b), in a parallel setup, each CPU is assigned a bin and its neighboring bins. For a two-dimensional simulation the neighborhood consists of 8 cells, while in a 3D setup the number of neighboring bins is 27. Bins cannot be shared among processors since two CPUs might assign the same particle to different collision partners. The latter could lead to erroneous data in the particle's post-collision properties. Once a CPU has completed the collision partner search it is assigned a new bin. As is illustrated in Fig.1(c), there are two possibilities how to progress the parallel search. One option is to let all processors wait until the last CPU has finished its scattering detection. New bins are then assigned to all CPUs at the same time. The second possibility is that a processor can move independently to another bin once it has finished its scattering partner search. However, it must be ensured

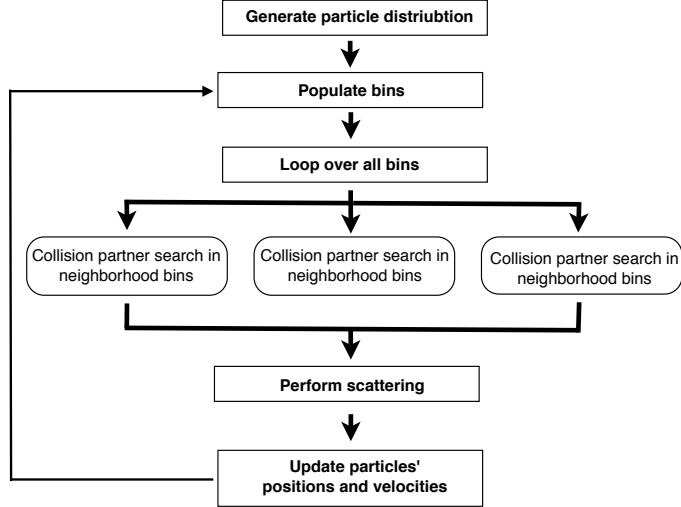


FIG. 2: Flow chart of particle simulation

that neither the new bin nor its neighborhood are part of the still ongoing collision detection of the other CPUs. For our work, we chose the first method.

Figure 2 gives a rough outline of the code structure. The simulation starts with the initialization of the particle distribution. Hereby, particles are assigned their spatial coordinates, velocities, and further properties which are required in the simulation, such as mass. The simulation space has a given spatial extension. Due to the self-similar nature of shock wave problems neither the coordinates nor the velocities are given specific physical units. The binning grid is set up with a chosen number of bins in each dimension. We couple the time step size Δt to a particle velocity v and the width of a bin Δx through:

$$\Delta t = \eta \frac{\Delta x}{v}. \quad (12)$$

Hereby, v is a large particle velocity in the simulation and can either be coupled to the initial velocity distribution or be the maximal particle velocity at each time step. By setting the travelled distance to be only a small fraction $\eta \ll 1$ of the bin-width, we ensure that particles do not leave their scattering neighborhood within Δt . At the beginning of each time step, the particles are sorted into the bins, whereas, for each bin, we determine the corresponding number of particles N_{bin} . The latter is used to calculate the effective radius of each particle in two or three dimensions:

$$r_{\text{eff},2D} = \frac{\Delta x^2}{2\lambda N_{\text{bin}}}, \quad r_{\text{eff},3D} = \sqrt{\frac{\Delta x^3}{\pi \lambda N_{\text{bin}}}}. \quad (13)$$

Within a loop over all bins, the collision partner search is performed in parallel following the criteria for scattering detection as discussed in section IV. Figure 3 shows the particle selection in one bin $N_{\text{bin}} \sim O(10^4)$ for a chosen particle of interest according to the discussed collision tests:

- Collision test 1: Check if $d_{\min} \leq (r_{\text{eff},A} + r_{\text{eff},B})$ during Δt
- Collision test 2: Determine the collision times $t_{c,1}$ and $t_{c,2}$ from a given λ
- Collision test 3: Choose final collision partners according to their smallest distance

With a chosen mean free path of $\lambda = 0.01\Delta x$, eq.(13) gives an effective particle radius of $r_{\text{eff},2D} = 5 \times 10^{-3}\Delta x$ which explains why only a few particles in Fig. 3 pass the second collision test. Figure 5 gives a comparison between the total number of particles N in the simulation and the number of possible collisions. All simulations were performed for particles with the same initial velocity but random directions of motion. For a total particle number of $N > 10^6$ we find that typically all particles in the simulation find a scattering partner.

Once collision partners are assigned to each other, we perform the scattering in the center of mass frame of each colliding pair. This is currently done in a Newtonian formalism but will be extended to include effects of Special Relativity in the future, as have been done in previous works [6, 7, 65]. The scattering angles can be calculated analytically for a given test-particle shape. However, due to the random nature of individual particle motion in bulk

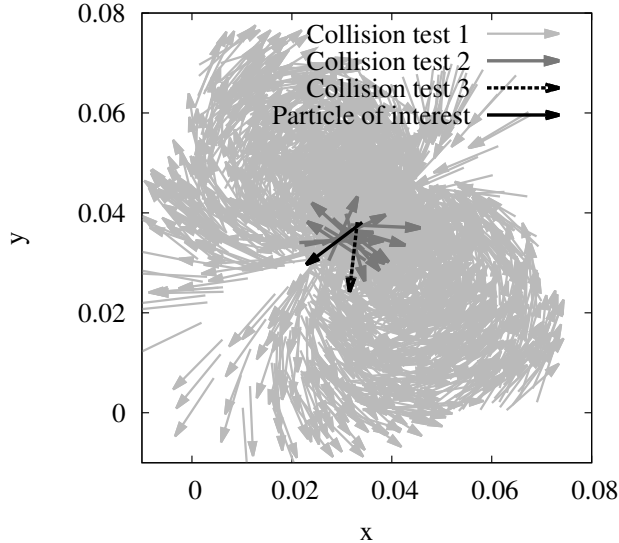


FIG. 3: Three collision tests, as discussed in the text, performed in one bin for a particle number of $N_{\text{bin}} \sim O(10^4)$, mean free path $\lambda = 0.01\Delta x$, velocity $v_i = 300$, and time step size $dt = 0.1 \Delta x/v_i$.

matter we chose a simpler approach by orienting the outgoing post-collision velocity vectors randomly and opposite to each other in space.

For the scattering of final collision partners, different methods can be considered. Due to the large number of particles it is not unlikely that two particles, A and C , find the same collision partner B . Such situation can be resolved in different ways, for example:

1. Scattering is only performed for two unambiguously determined collision partners
2. Only one out of two conflicting scattering processes is performed
3. Both scatterings are performed consecutively

For the last case, the second scattering process involves the updated particle as collision partner, i.e. the latter has a new velocity vector as a result of the first interaction. Figure 4 shows collision partners with their pre- and post-collision velocity vectors for the above scenarios. The scattering partners are visualized through a connection by a thin dashed line. The mean free path was chosen to $\lambda = 0.01\Delta x$. With a number of particles per bin of $N = 76$, this leads to an effective radius of $r_{\text{eff}} \sim 0.66 \Delta x$, which is large enough to ensure that typically every particle in the simulation should find a scattering partner.

Note, that in the first scenario which is shown in figure 4 (a) many particles do not undergo collisions. In these cases an interaction partner was found. However, the search was in conflict with another particle's collision detection which determined the same particle as its scattering partner. As a result, no scattering was performed for all three particles. Such "ring structures" were noticed in previous studies and were shown to be able to lead to an underestimation of the collision rate [7]. Though Fig. 5 shows that the percentage of non-interacting particles seems to stay constant with growing particle number, the likeliness of conflicts in collision detection could increase for higher values of N . This could lead to problems in calculations aimed to describe dense systems in equilibrium. Instead of frequent particle interaction, the collision rate could decrease due to a growing number of scattering conflicts.

Concerning the collision rate, the second approach for final collision partner search is more effective. Here, one of the two scatterings in conflict is performed and, as can be seen in Fig. 4 (b) and Fig. 5 the number of non-interacting particles is lower. Figure 4 (c) shows that for the third scenario we find that all particles are involved in scattering processes. With interactions in conflict being performed sequentially, the only possible scenario for which a possible interaction would be omitted is a situation in which particle A finds a scattering partner B , while the latter detects particle C as more suitable for a collision, and particle C does not interact at all. This case is very unlikely and we don't find its occurrence in our simulations.

For all three scattering criteria, the final collision partners are chosen according to the smallest distance. For comparison we also performed tests for the determination of the final scattering partner via the shortest collision time t_c . The resulting collision partners are shown in Fig. 4 (d). It can be seen that, unlike for the smallest distance, interacting test-particles are generally farther away from each other. In case of large bin-widths or small values of λ ,

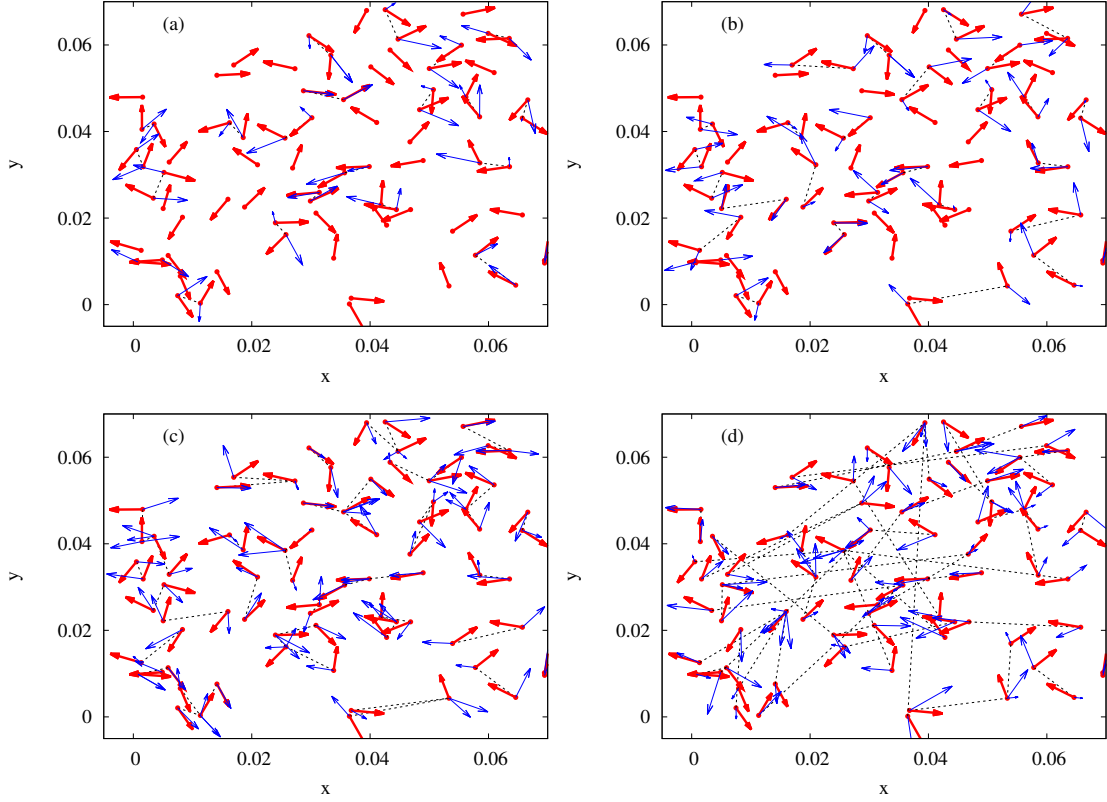


FIG. 4: Result of the scattering partner search with $N_{\text{bin}} = 76$, $\lambda = 0.01\Delta x$, $v_i = 300$, and $\Delta t = 0.1\Delta x/v_i$. Pre- and post-collision velocity vectors are illustrated by thick and thin lines, respectively. Collision partners are connected by a thin dashed line. (a) Unambiguously determined collision partners, (b) one out of two collisions in conflict is performed, (c) all collisions are performed. (d) Final collision partners are determined according to the shortest collision time.

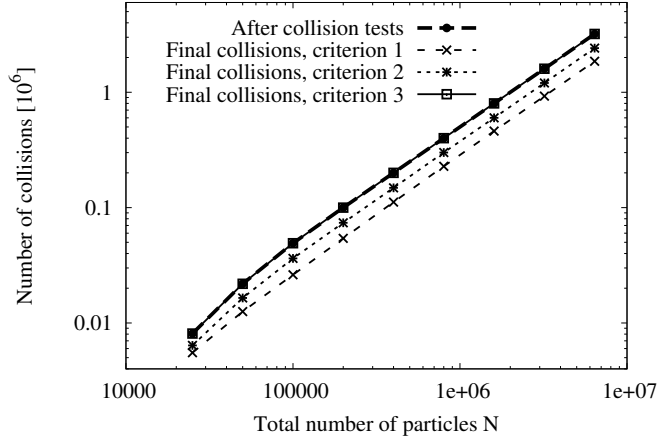


FIG. 5: Possible collisions according to final collision criteria shown in Figs.4 (a) - (c) as a function of total particle number N . The number of final collisions is compared to all possible collisions in the simulation. The latter contain interactions which are in conflict with each other.

such an algorithm for collision detection could decrease the spatial resolution in a simulation. For shock wave studies a failure to sufficiently spatially localize scattering partners could result in artificial broadening of the shock front. Therefore, to achieve a high resolution in our simulations we determine the final collision partner according to the closest distance.

Once scattering has been performed for all colliding particles, we update the particle velocities and positions. For the latter, we distinguish between positive and negative collision times. As mentioned before, large particle densities

and small mean free paths can cause the particles' effective radii to overlap. This results in negative collision times according to eq.(10). In such a case we treat the particle collision as instantaneous and update the particle positions via:

$$x(t + \Delta t) = x(t) + v_{\text{new}} \Delta t, \quad (14)$$

where v_{new} is the post-collision velocity. For particles with positive collision times t_c the new position is:

$$x(t + \Delta t) = x(t) + v_{\text{old}} t_c + v_{\text{new}} (\Delta t - t_c) \quad (15)$$

where v_{old} is the pre-collision velocity.

In the next section we will present results of hydrodynamic shock wave studies performed with the kinetic test-particle code.

VI. SIMULATIONS IN THE HYDRODYNAMIC LIMIT

As mentioned in the introduction, an advantage of kinetic approaches is their ability to capture the behavior of matter for all Knudsen numbers. In this work we want to test the capability of our scattering partner search algorithm to reproduce hydrodynamic behavior, i.e. matter with small Knudsen numbers, especially with regard to the evolution of shock waves. The latter are often used as test cases to study the capability of a hydrodynamic code to capture steep gradients and discontinuities. Furthermore, most test problems possess analytic solutions which allow the user to quantify and compare the performance of different codes. The test suite which we present in this work consists of the following problems: the Sod test, a classical Riemann problem to show our code's ability to propagate shock waves and satisfy the shock jump conditions, and the Noh problem to test the conversion of kinetic in internal energy and shock wall-heating. We chose the Sod and Noh tests for the following reasons: the Sod test is generally considered to be an elementary benchmark test that all codes designed to model hydrodynamic shockwave propagation should pass [66] and the Noh problem [67] tests the ability of our code to model the evolution of shocks in imploding systems similar to supernovae or ICF capsule systems that we aim to study.

Our studies are typically carried out with $\sim 10^7$ test-particles placed in a simulation box which has reflective boundary conditions and is divided into $(10^4 - 10^6)$ equally sized bins. To ensure hydrodynamic equilibrium by frequent interaction of particles, their mean free path is chosen to be a small fraction of the distance which the test-particles can traverse in a given timestep Δt . In the present study, interactions are only modeled in the form elastic scattering. As a consequence, the resulting matter behaves as a dense gas with the number of degrees of freedom f given by the number of dimensions in the simulation. The heat capacity ratio $\gamma = 1 + 1/f$ becomes $\gamma = 2$ for a two dimensional simulation and $\gamma \sim 1.67$ in the case of three dimensions. The quantities which are calculated and compared to analytical solutions are the particle number density n , pressure p , and bulk velocity v_b .

The density is given simply by the number of particles per corresponding volume N_V/V while the bulk velocity of matter is determined via:

$$v_b = \frac{1}{N_V} \sqrt{v_{b,x}^2 + v_{b,y}^2 + v_{b,z}^2}, \quad v_{b,\alpha} = \sum_{i=1}^M v_{i,\alpha}, \quad (16)$$

whereas $\alpha = x, y$, and z . The particle velocities are also used in the determination of the pressure from the stress tensor of dense gases: [68, 69]:

$$\mathbf{P}_{\alpha\beta} = - \left(\sum_i m (v_{i,\alpha} - v_{b,\alpha}) (v_{i,\beta} - v_{b,\beta}) + \frac{1}{2} \frac{1}{\Delta t} \sum_i \sum_{i \neq j} r_{ij,\alpha} \Delta p_{i,\beta} \right), \quad (17)$$

with $\vec{r}_{ij} = \vec{r}_i - \vec{r}_j$ and $\Delta \vec{p}_i = m (\vec{v}_{i,\text{new}} - \vec{v}_{i,\text{old}})$ being the change in momentum of particle i due to interaction with particle j . The stress tensor is composed of a kinetic and a potential part. Hereby, the first term in eq.(17) is the kinetic contribution. It dominates for gases and is induced by the momenta carried by the particles around their bulk motion. It is also the part of the stress tensor which results in the usual thermal pressure $p = k_b T N/V$ with k_b being the Boltzmann constant. The second contribution is the potential part which arises due to momentum transfer from particle interaction and dominates the pressure in liquids. Applying eq.(17) to bulk matter with a volume V results in a corresponding pressure of:

$$p_{2D} = -\frac{1}{V} \frac{\mathbf{P}_{xx} + \mathbf{P}_{yy}}{2}, \quad p_{3D} = -\frac{1}{V} \frac{\mathbf{P}_{xx} + \mathbf{P}_{yy} + \mathbf{P}_{zz}}{3}. \quad (18)$$

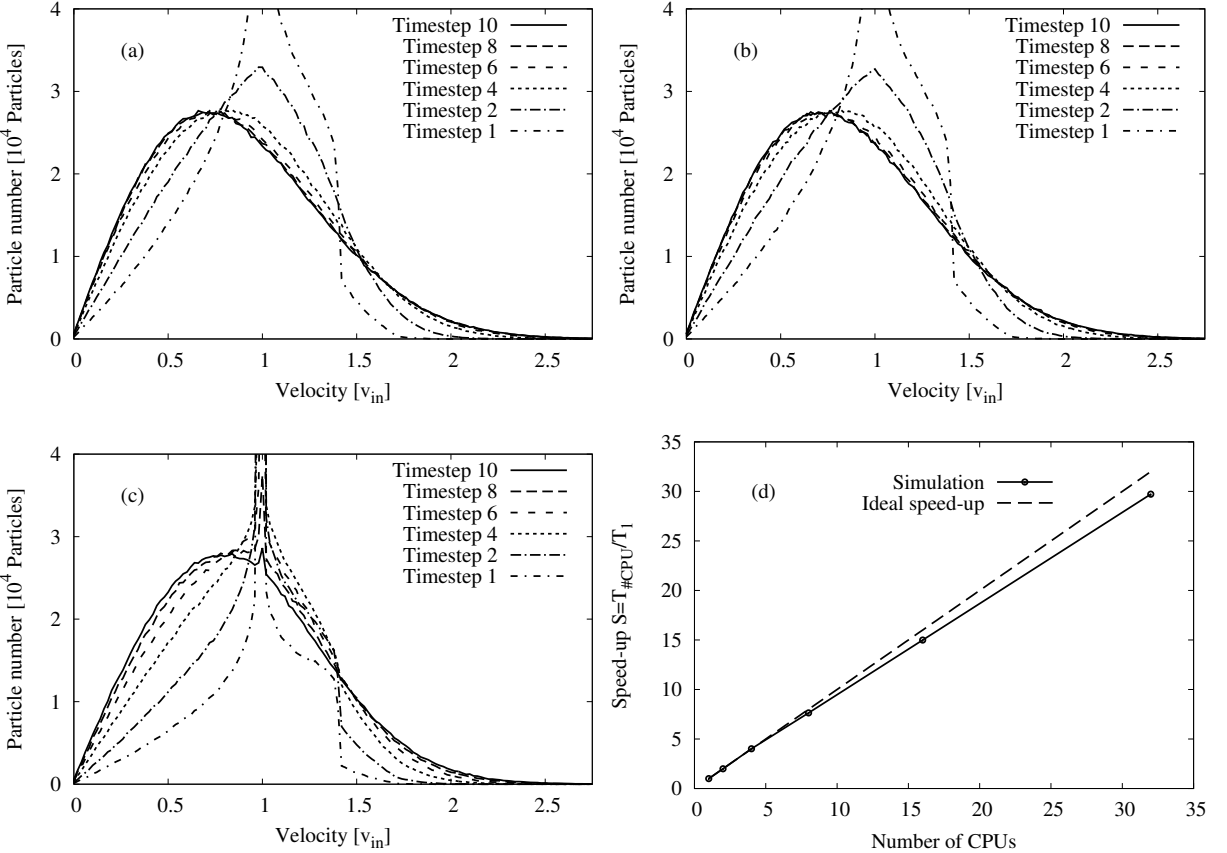


FIG. 6: Maxwell-Boltzmann distribution. $M = 1.6 \times 10^6$, 100×100 bins. From left top to right bottom: (a) $\lambda = 0.01 \Delta x$ (b) $\lambda = 0.1 \Delta x$, (c) $\lambda = 1.0 \Delta x$ (d) Scaling of the equilibration study with number of processors applying $\lambda = 0.01 \Delta x$

Given the symmetries of the simulated system, we calculate averages of n , p , or v_b for a given interval of distance, e.g. distance Δx or radial distance Δr . In addition, number density, pressure, and bulk velocity are also determined as averages in sample bins. The grid used to define the sample bins does not have to be identical to the grid that defines the scattering bins. The number of sample bins can be chosen much larger for a high resolution data output if desired.

A. Equilibration and CPU timing

To study the equilibration rate in dependence of the test-particle mean free path, we set up a two-dimensional simulation space with $N = 1.6 \times 10^6$ particles distributed homogeneously over 100×100 bins. All particles are initialized with the same initial absolute velocity v_{in} and random orientation of the velocity vector. Varying the mean free path from $\lambda = 0.01 \Delta x$, $0.1 \Delta x$, to $1.0 \Delta x$, we determine the particle velocity distribution over the first ten time steps. For systems in equilibrium the latter should promptly reach the Maxwell-Boltzmann distribution. Figures 6(a)-6(c) show the number of particles as a function of absolute velocity for different values of λ . It can be seen that simulations with $\lambda = 0.01 \Delta x$ and $\lambda = 0.1 \Delta x$ obtain the Maxwell Boltzmann velocity distribution within the first 6-10 time steps, while for mean free paths $\lambda \gtrsim 1.0 \Delta x$ the equilibration time is longer. This is a motivation for us to apply small values of $\lambda \lesssim 0.1 \Delta x$ in simulations which aim to describe equilibrium configurations.

As discussed in sections IV and V, our scattering partner search algorithm is designed to work in parallel. To test the speed-up we performed timing tests for the first ten timesteps of the above velocity equilibration study using $\lambda = 0.01 \Delta x$. The computational speed-up is defined as $S = T_{\#CPU} / T_1$, where $T_{\#CPU}$ is the wall-clock performance time of an algorithm with $\#CPU$ number of processors, while T_1 is the time when only one processor is used. The results for $\#CPU = 1 - 32$ are shown in figure 6(d) which gives as comparison also the case of ideal speed-up with $S = \#CPU$. Though the performed simulations show a deviation from the latter with increasing number of processors the overall speed-up is still close to an ideal behavior and therefore promising for implementations of our

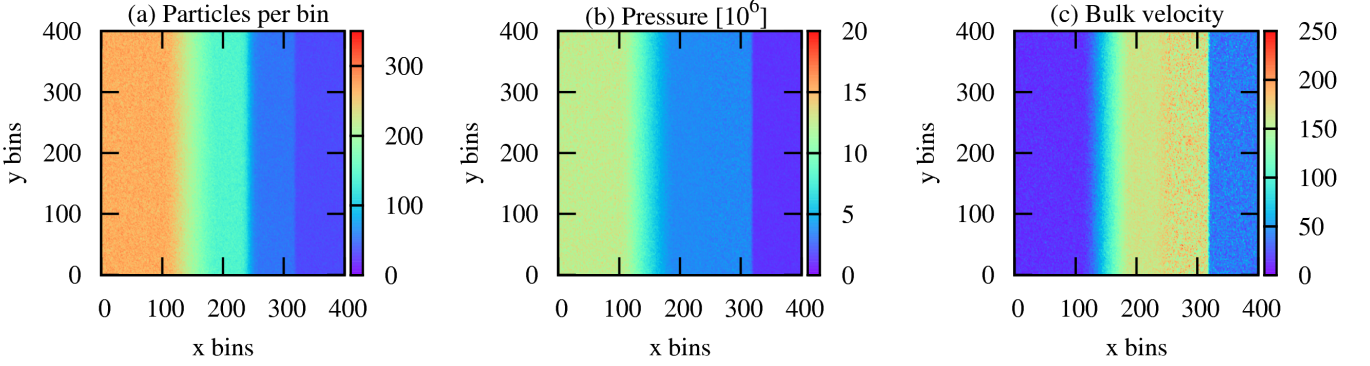


FIG. 7: 2D Sod shock test: $N = 2.4 \times 10^7$ test-particles are distributed over 400×400 bins with $\lambda = 0.01\Delta x$ and $\Delta t = 0.25\Delta x/v_R$. (a) Particle number per bin, (b) pressure, and (c) bulk velocity with developed shock profiles at timestep $t = 350 \Delta t$

algorithm on larger systems with thousands of cores. It should however be noted that the CPU scaling shows such a good performance due to the homogeneous distribution of test-particles and thereby equal load of all processors. For physical problems which involve a large number of particles concentrated in only a few bins and therefore not distributed over all CPUs the scaling will be worse. Possible solutions to ensure a more homogeneous processor load include the usage of adaptive grids or the individual CPU update of the active bins as discussed in section V.

B. Sod test

We start our series of shock wave studies with the Sod shock-tube test [66]. It is a classical a Riemann problem and has been performed by various hydrodynamic and kinetic algorithms (see e.g. [70–77]). The simulation space is divided into two equally sized parts with different pressures and densities on both sides. The ratios of the left- and right-hand side pressures, number densities, and bulk velocities are set to:

$$(n, p, v_b)_L = (1, 1, 0), \quad (n, p, v_b)_R = (0.125, 0.1, 0). \quad (19)$$

Initially, both box partitions are separated. At the start of the simulation, the separation wall is removed which leads to the development of a shock front that propagates from the high density into the low density matter. The shock front is followed by a contact discontinuity and a rarefaction fan. The latter is visible in the pressure as well as the density profiles, while the contact discontinuity manifests itself only in the density distribution.

Our first simulation is carried out with $N = 2.4 \times 10^7$ particles in two dimensions. The size of the simulation space spans over $0 \leq x, y \leq 7$ and is divided into 400×400 bins. We initialize the particle velocities with $v_R = 300$ and $v_L = 268.32$, while the particle density ratios are set up as in eq.(19). With a chosen particle mean free path of $\lambda = 0.01 \Delta x$ and a timestep size of $\Delta t = 0.25 \Delta x/v_R$ the particle velocities equilibrate to the Maxwell-Boltzmann distribution within the first time steps. After 20 time steps the partition wall is removed and we observe the evolution of a shock front which propagates from the right into the low density and low pressure region on the left.

Figure 7 shows the particle number per bin, the pressure, and the bulk velocity at timestep $t = 350 \Delta t$. To compute the corresponding profiles as a function of distance x , we average the density and pressure over bins in the y -direction, while the bulk velocity is computed via eq.(16) with averaged v_x and v_y . The resulting profiles are then compared to the analytic solutions which are obtained using the *exact_riemann.f* code [78]. We plot the results for density, pressure, and bulk velocity in Figs. 8(a) - 8(c), whereas the density and pressure are normalized by their initial values n_L and p_L . We find that the simulation agrees well with the analytic solutions. Disagreement can be found in the sharpness of the contact discontinuity in the particle number density. The latter is accompanied by an increase in the bulk velocity, an effect which has also been observed in other kinetic approaches [72, 79] and could be connected to the particle mean free path [80]. Statistical fluctuations can be found in all quantities but are expected to decrease for larger particle numbers.

Results for the three-dimensional Sod shock tube test are shown in Fig. 9 and Fig. 10. For better comparison with the two dimensional calculation, we set up the same particle densities by dividing the simulation space into $400 \times 20 \times 20$ bins and keeping the bin-widths as well as the particle numbers the same as in the 2D case. The resulting density, pressure, and bulk velocity profiles are presented in Figs. 10(a) - 10(c). The results are qualitatively very similar to the two dimensional simulations whereas the heights of the pressure and density plateaus are modified due to

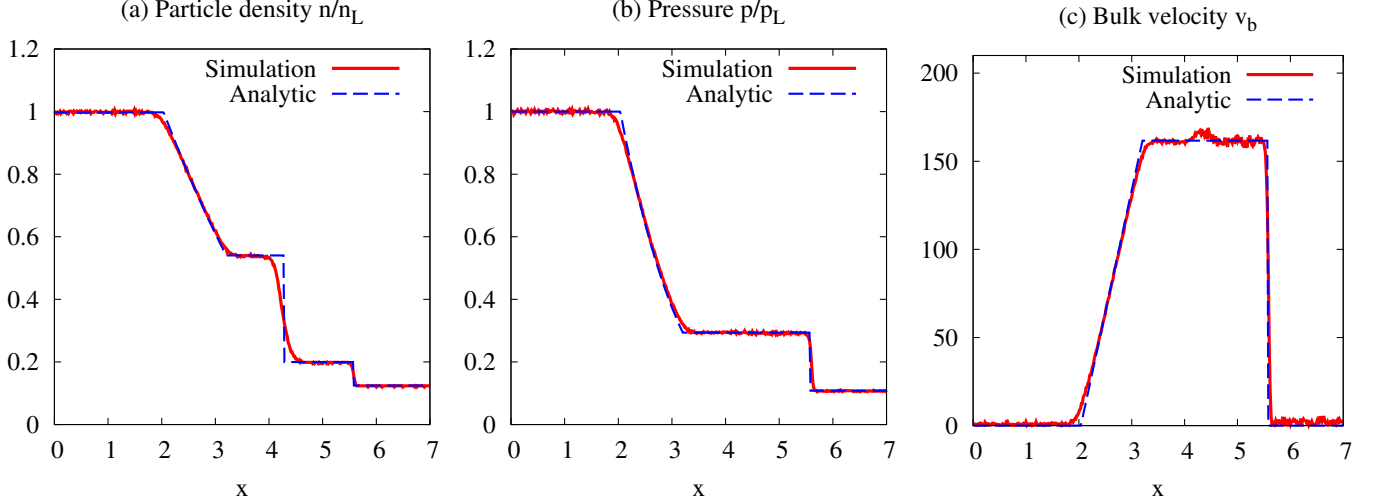


FIG. 8: 2D Sod shock test as in Fig. 7. Profiles of (a) normalized density, (b) normalized pressure, and (c) bulk velocity at $t = 350 \Delta t$ are shown together with the analytical solutions.

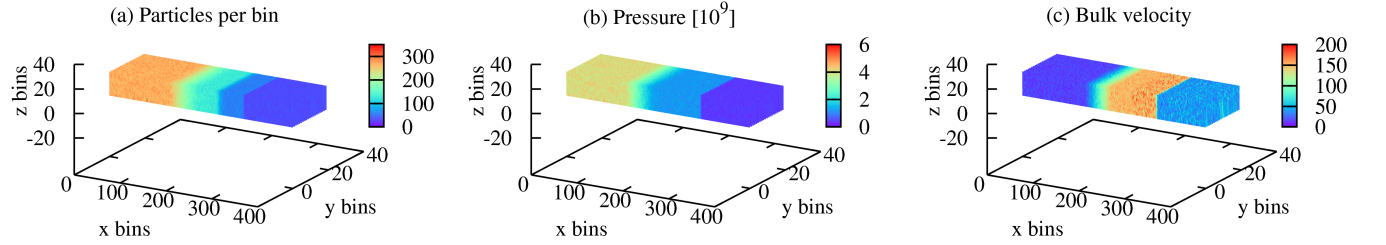


FIG. 9: 3D Sod shock test: $N = 2.4 \times 10^7$ test-particles are distributed over $400 \times 20 \times 20$ bins with $\lambda = 0.01 \Delta x$ and $\Delta t = 0.25 \Delta x/v_R$. (a) Particle number per bin, (b) pressure, and (c) bulk velocity with developed shock profiles at timestep $t = 350 \Delta t$.

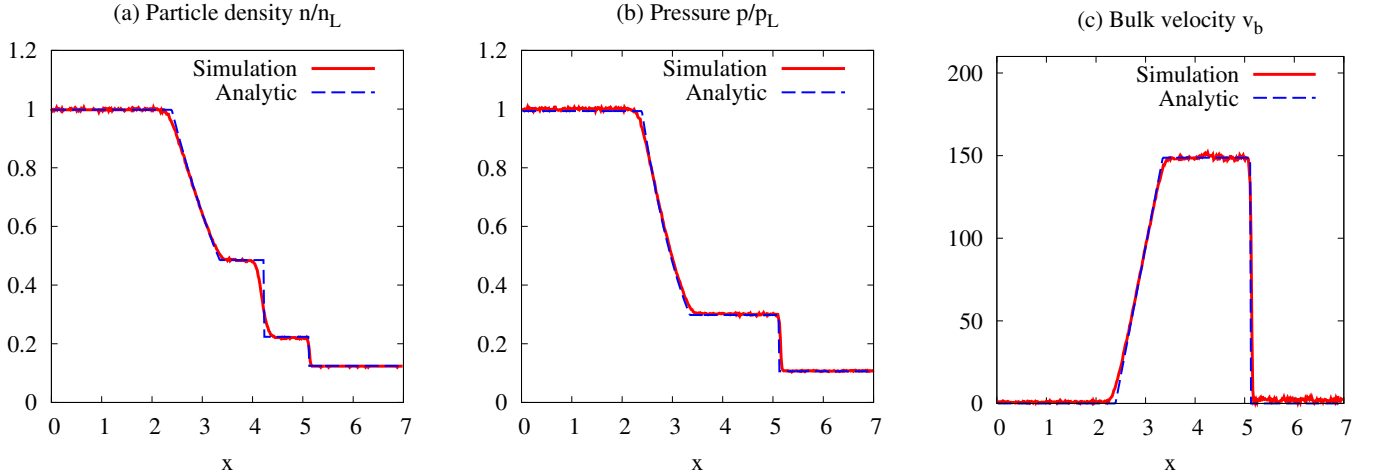


FIG. 10: 3D Sod shock test as in Fig. 9. Profiles of (a) normalized density, (b) normalized pressure, and (c) bulk velocity at $t = 350 \Delta t$ are shown together with the analytical solutions.

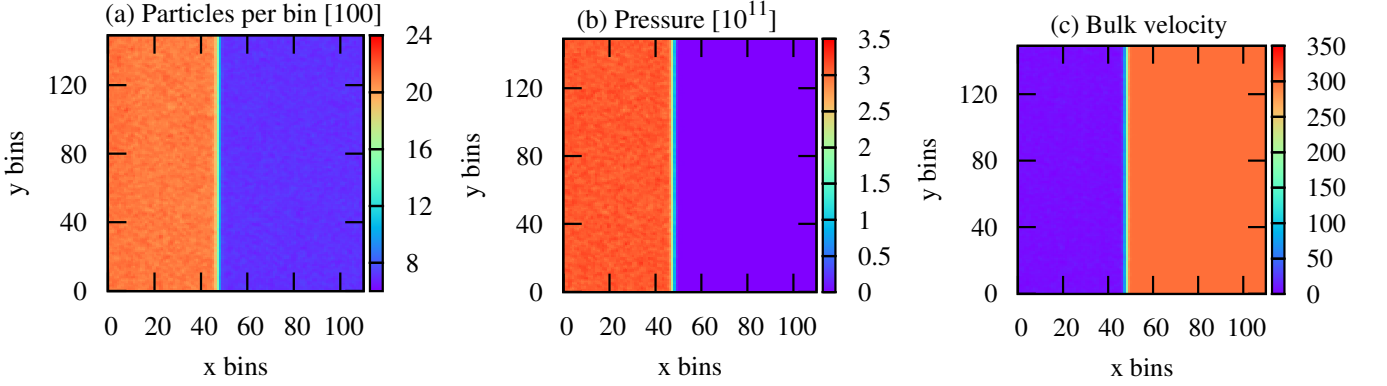


FIG. 11: Planar Noh test in 2D: $N = 3.2 \times 10^7$ test-particles distributed over 300×150 bins with $\lambda = 0.01 \Delta x$ and $\Delta t = 0.25 \Delta x/v_{\text{in}}$. (a) Particle number per bin, (b) pressure, and (c) bulk velocity at timestep $t = 380\Delta t$ with developed shock profiles.

the different heat capacity ratio of $\gamma \sim 1.67$ for a three dimensional system. Again, it can be seen in Fig. 10 that the analytical solutions are well reproduced by the test-particle approach. This has also been demonstrated in other kinetic simulations [72–77]. With that, we turn to the Noh test which is a more challenging problem for hydrodynamic simulations.

C. Noh test

The Noh or Newtonian wall shock problem [67] is an important test for approaches which aim to study collapsing, i.e. imploding systems. While being performed by hydrodynamic codes [81], the Noh problem has not been analyzed in many particle based approaches, and is therefore of special interest for our study. The test is initialized in form of a gas with homogeneous density n_{in} that streams with a uniform velocity v_{in} towards a wall of the simulation box or its origin. As matter starts to pile up, it converts kinetic into internal energy. An accretion shock front forms enclosing the shocked matter, whereas its radius as a function of time is given by:

$$r_{\text{shock}}(t) = \frac{1}{2} (\gamma - 1) v_{\text{in}} t. \quad (20)$$

The resulting density profile can be written as a function of distance r :

$$n(r) = n_0 \left(\frac{\gamma + 1}{\gamma - 1} \right)^d, \quad r < r_{\text{shock}} \quad (21)$$

$$n(r) = n_0 \left(1 + \frac{v_{\text{in}} t}{r} \right)^{d-1}, \quad r \geq r_{\text{shock}}. \quad (22)$$

Hereby, d gives the geometry of the system with $d = 1$ for a planar, $d = 2$ for a cylindrical, and $d = 3$ for a spherical setup. Many hydrodynamic simulation codes experience problems with the Noh test due to anomalous wall-heating which decreases the density of matter close to the wall of the simulation box [67, 81].

We performed the Noh test in planar as well as cylindrical geometry with a total particle number of $N = 3.2 \times 10^7$ and $v_{\text{in}} = 300$. For planar simulation we divide the simulation space into 300×150 bins with $0 \leq x \leq 5.26$ and $0 \leq y \leq 2.625$. The mean free path is chosen to $\lambda = 0.01 \Delta x$ with a timestep size $\Delta t = 0.25 \Delta x/v_{\text{in}}$. The number of particles, pressure, and bulk velocity per bin at $t = 300 \Delta t$ are given in Fig. 11. The figures show the shocked high density matter composed of particles which are streaming from the right-hand side of the simulation box and accumulate along the left wall. Figures 12(a) - 12(c) give the corresponding normalized particle densities, pressures, and bulk velocities averaged over the y-dimension. Generally the results of the simulation are in good agreement with the analytical solution. The latter was obtained by the *noh.f* code from [78]. The particle density of the shocked matter is slightly under-predicted and the shock front is again broader than in the analytic solution. However, as can be seen in Fig. 13, the density profiles are sensitive to N_{bin} and approach the analytic solution when its values are increased.

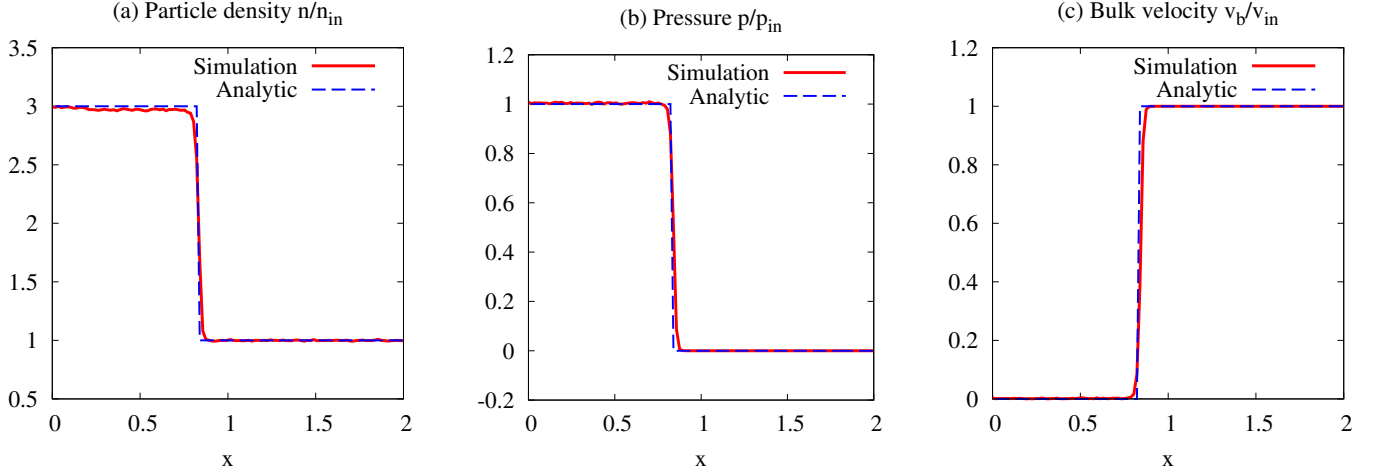


FIG. 12: Planar Noh test in 2D as in Fig. 11. Profiles of (a) normalized density, (b) normalized pressure, and (c) bulk velocity at $t = 380 \Delta t$ are shown together with the analytical solutions.

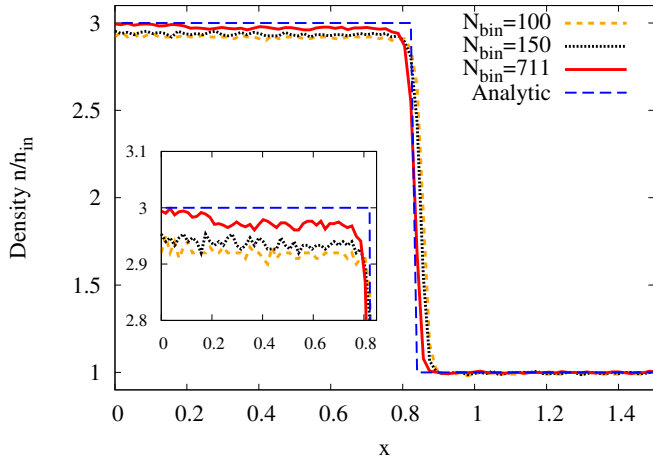


FIG. 13: Noh test for a two dimensional setup as described in Fig. 12 with different values of particles per bin N_{bin} .

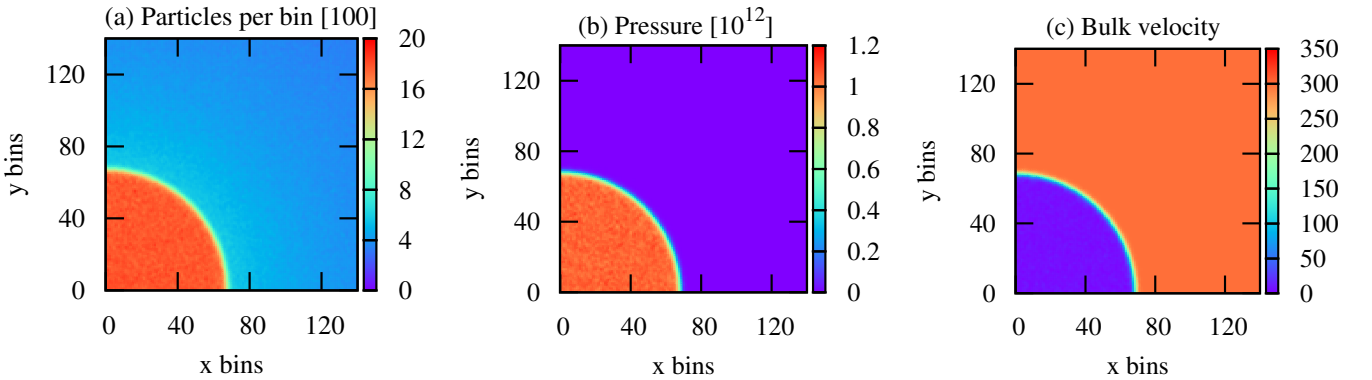


FIG. 14: Cylindrical Noh test in 2D: $N = 3.2 \times 10^7$ test-particles distributed over 200×200 bins with $\lambda = 0.01 \Delta x$ and $\Delta t = 0.25 \Delta x / v_{in}$. (a) Particle number per bin, (b) pressure, and (c) bulk velocity at timestep $t = 270 \Delta t$ with developed shock profiles.

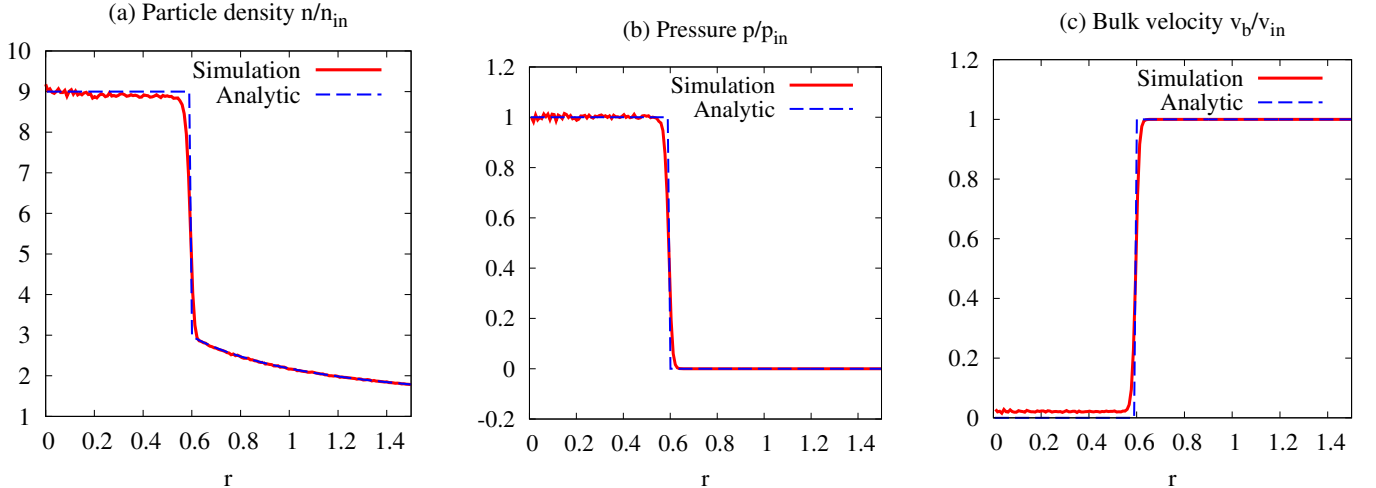


FIG. 15: Cylindrical Noh test in 2D as in Fig. 14. Profiles of (a) normalized density, (b) normalized pressure, and (c) bulk velocity at $t = 270 \Delta t$ are shown together with the analytical solutions.

In Fig. 14 and 15 the results of the cylindrical Noh test are shown. The simulations space is now divided into 200×200 bins with $0 \leq x, y \leq 3.5$, whereas timestep size and mean free path are the same as for $d = 1$. The particle number per bin, pressure, and bulk velocity are shown in Fig. 14. Different to the Noh test in planar geometry, particles now stream with uniform radial velocity towards the origin of the simulation. The density, pressure, and velocity averages are also taken over the radial distance r . Again, we find good agreement between analytical prediction and kinetic simulation as shown in Fig. 15(a) - Fig. 15(c), while small deviations are present in the particle density and the width of the shock front. In addition, for the shocked matter, the bulk velocity in Fig. 15(c) seems to be above zero. The reason for this lies in our approach to calculate v_b . For the cylindrical Noh test we first determine the bulk velocity according to eq.(16) for every bin and then calculate its radial average. As a consequence, possible negative and positive fluctuations in v_x and v_y for different bins do not average out but are summed and thereby lead to positive fluctuations of v_b . The latter, averaged over radial distance, results in the observed bulk velocity above zero. An increase of the bin-width or the number of test-particles per bin N_{bin} should improve the statistics and reduce the bulk velocity. An alternative approach is to determine the radial velocity:

$$\vec{v}_r = \frac{1}{N_V} \sum_{i=1}^M \vec{v}_i \cdot \vec{r}_i / r_i \quad (23)$$

instead. It is a function of radial distance r and can have positive and negative values. Thereby fluctuations of \vec{v}_r can cancel out when averaged over several bins, leading to the expected $\vec{v}_r \sim 0$ for shocked matter. However, for both, the planar as well as cylindrical Noh tests, it is noteworthy that no signs of wall-heating are observed. It will be interesting to see if this observation stays invariable for even higher particle numbers and how it compares to other particle based simulations.

VII. SIMULATIONS OF NON-EQUILIBRIUM SYSTEMS

As mentioned in the introduction, an important advantage of kinetic schemes is their ability to simulate systems which have large Knudsen numbers and are therefore not equilibrium. In this section, we want to test this regime within our approach using particle mean free paths that are larger than a characteristic length scale of the system $\lambda > L$. We choose $L = 3 \Delta x$ since it defines a particle's scattering neighborhood and study two representative values of $\lambda = 4 \Delta x$ and $\lambda = 32 \Delta x$. Both are applied to shock tests which were previously discussed in sections VI B and VI C, whereas we compare the results to the equilibrium regime with $\lambda = 0.01 \Delta x$ and the free-streaming case. For the latter the particles do not interact with each other and their mean free path can be assumed as infinitely large. As representative cases for the shock simulations we choose the 2D Sod test and the 2D planar Noh test, whereas we expect the results for the 3D Sod test and the cylindrical Noh test to be qualitatively similar. Mean free path studies of the Sod test have also been performed by e.g. [6, 80] whereas we are not aware of any similar studies with the Noh problem.

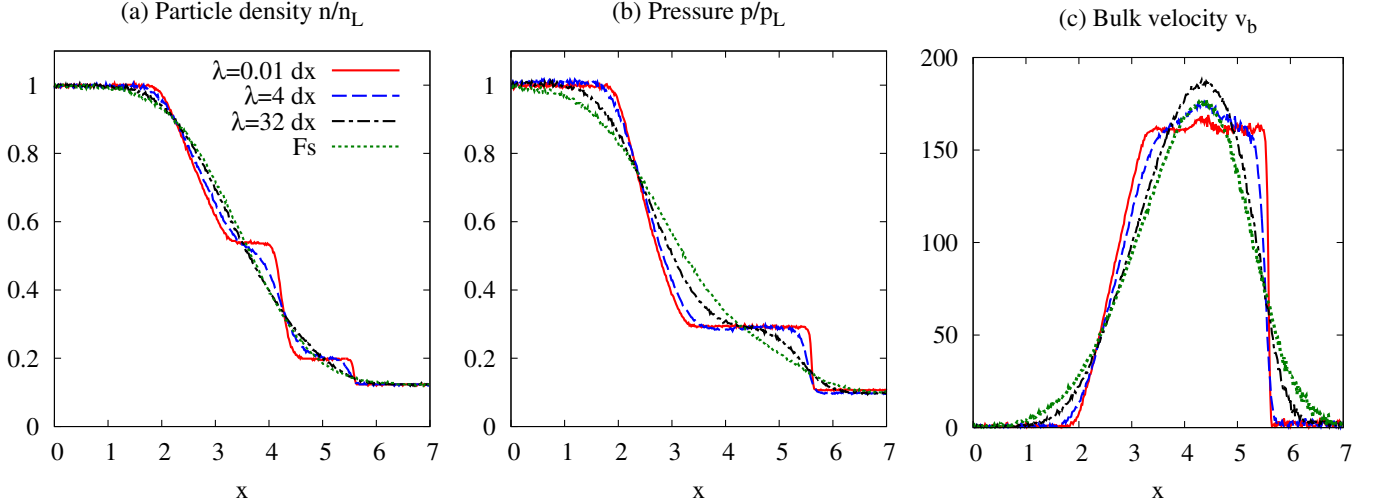


FIG. 16: 2D Sod shock test as in Fig. 7. Profiles of (a) density, (b) pressure, and (c) bulk velocity at $t = 350 \Delta t$. The mean free path is varied from $\lambda = 0.01 \Delta x$, $4 \Delta x$ to $32 \Delta x$. The simulation using free streaming particles is marked by Fs.

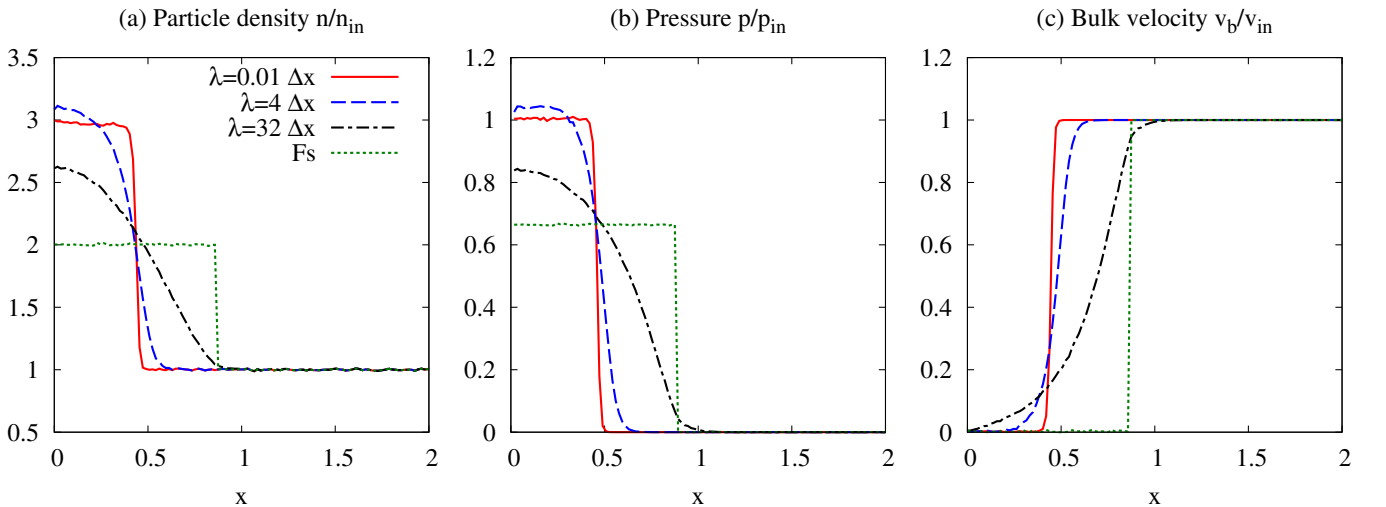


FIG. 17: 2D Noh shock test as in Fig. 12 in planar geometry and $N = 1.6 \times 10^7$. Profiles of (a) density, (b) pressure, and (c) bulk velocity at $t = 200 \Delta t$. The mean free path is varied from $\lambda = 0.01 \Delta x$, $4 \Delta x$ to $32 \Delta x$. The simulation using free streaming particles is marked by Fs.

We perform the Sod test with $N = 2.4 \times 10^7$ test-particles, 400×400 bins, and $-3.5 \leq x, y \leq 3.5$. The initialization process is the same as in section VII B. For the first twenty timesteps the particle system equilibrates to the corresponding Maxwell-Boltzmann velocity distributions whereas the test-particle mean free paths are $\lambda = 0.01 \Delta x$. At $t = 20 \Delta t$, the partition wall between the high and low density matter is released and the particle mean free paths are set to their new values of $\lambda = 4 \Delta x$ and $\lambda = 32 \Delta x$, respectively. The results are shown in Fig. 16(a) - Fig. 16(c). We plot the density, pressure, and bulk velocity averaged over the y -dimension. It can be seen that for $\lambda = 4 \Delta x$ the density, pressure, and velocity profiles are significantly washed out, however, they still indicate the general features of the Sod shock. For $\lambda = 32 \Delta x$, on the other hand, almost no shock features are visible. The density profile is very similar to the free-streaming regime, whereas the pressure profiles still reproduce a small plateau near the contact discontinuity.

Similar behavior can be observed for the Noh test in Fig. 17(a) - Fig. 17(c). As before, we plot the density, pressure, and bulk velocity profiles as functions of the distance x . The simulation space is set up with $N = 1.6 \times 10^7$ test-particles in 300×150 bins, where $0 \leq x \leq 5.25$ and $0 \leq y \leq 2.625$. The timestep size and the initial particle velocity are the same as in section VII C. Like in the Sod mean free path test, it can be seen that with increasing

values of λ , the shock front broadens. This can be attributed to particles which, once they reach the shocked matter region, are not trapped by in-flowing particles, but can escape due to their large mean free path. While the peak density and pressure for $\lambda = 4 \Delta x$ are higher than in the equilibrium case, the opposite behavior can be found for $\lambda = 32 \Delta x$. A possible reason is that for $\lambda = 4 \Delta x$ more particles reach the wall of the simulation box at $x = 0$. Here, they can become trapped due to scattering with in-flowing particles which leads to a higher particle number. If the mean free path is set to larger values of $\lambda = 32 \Delta x$, the majority of particles does not interact and, after being reflected on the walls of the simulation box, propagates back to larger distances. As can be expected, this behavior is even more pronounced in the free streaming regime. This results in densities twice as large as the initial value and zero bulk velocity. The latter is a consequence of the cancellation between the bulk velocities of in- and out-flowing test-particles. The non-zero pressure stems from the first term in eq.(17) and is due to the non-vanishing individual particle motion versus the zero total bulk velocity.

VIII. SUMMARY AND CONCLUSION

In this work we introduce and discuss a Monte Carlo kinetic scheme which simulates the phase space evolution of systems that can move in and out of hydrodynamic equilibrium. The code operates with test-particles that interact with each other via two-body collisions with variable particle mean free paths. To achieve high computational efficiency, the code is written in a parallel form and applies spatial binning of test-particles. We determine the interaction partners using the distance of closest approach while the final collision partners are chosen according to the shortest distance between them. Both deviations from the usual Direct Simulation Monte Carlo techniques, which determine interaction partners randomly from a scattering cell, are aimed to enhance spatial accuracy which could otherwise be compromised due to scattering partners which are far away from each other.

For first performance studies of our kinetic scheme we apply timing and mean free path tests with a simple gas of test-particles moving in two dimensions and interacting with each other via binary collisions. With equal initial absolute values, the test-particle velocities quickly equilibrate to the Maxwell-Boltzmann distribution when the particle mean free path is chosen small with respect to the distance which can be travelled by a particle within one timestep. Larger mean free paths on the other hand, lead to longer equilibration times. In addition, for this simple setup we find that the computational speed-up of the scattering partner search with the number of processors shows almost ideal behavior.

To further explore the capability of our kinetic scheme to reproduce hydrodynamic behavior as well as handle steep gradients and discontinuities, we apply shock wave tests in fixed-volume and imploding systems. These are the Sod and the Noh tests which we perform with 2.4×10^7 and 3.2×10^7 test particles, respectively, and compare the evolution of the resulting shock structures to the corresponding analytic solutions. Generally, we find good agreement between the predicted shock profiles and the results of the kinetic simulations. Common deviations are found in the sharpness of the shock fronts whereas these improve when larger particle numbers are used. Finally, we test the ability of the kinetic particle scheme to evolve systems which are not in hydrodynamic equilibrium. We perform the Sod and the Noh tests applying particle mean free paths which are much larger than the distance which a test-particle can travel within one timestep. As expected, we find that larger particle mean free paths lead to a more pronounced broadening of the shock front whereas the solutions approach the free streaming limit.

We can conclude that the particle kinetic scheme is capable to reproduce hydrodynamic behavior, especially with regard to shock wave evolution. More importantly, it can also simulate systems which are not in hydrodynamic equilibrium by applying large particle mean free paths. With this, it is an interesting tool to study systems such as core-collapse supernovae where neutrinos traverse from the trapped to the free streaming regime as well as the dynamics of ICF capsules where components of the nuclear fuel, such as thermal deuterons, posses mean free paths which are far too large relative to characteristic length scales of the region of thermonuclear ignition to assume hydrodynamic equilibrium.

IX. OUTLOOK

Future applications of our code in e.g. core-collapse supernova simulations will require further performance studies such as additional shock tests in two and three dimensions as well as studies concerning the ability of the particle approach to reproduce turbulent fluid motion, for example Rayleigh-Taylor and the Helmholtz instabilities. The search for scattering partners has to be upgraded to be able to handle particles moving at relativistic speeds. Also, three dimensional simulations will require higher particle numbers than were applied in the current study of $N \sim 10^8 - 10^9$ test-particles. To handle such large particle numbers, the scattering partner search has to be set up with distributed memory parallelization to enable the usage of $\gg 10^2$ processors. Corresponding CPU timing tests have to be performed

whereas large simulations would benefit from additional extensions such as adaptive grid and time step sizes for a better handling of shocks and large particle numbers. Another important implementation for future applications are the usage of additional test-particle interaction forces and realistic particle scattering cross-sections, e.g. nuclear forces and neutrino interactions with nuclear matter in core-collapse supernovae, as well as the handling of long-range forces such as gravitation. Finally, we plan to provide the scattering partner search code in form of a library to be applicable in a variety of studies of different hydrodynamic and transport problems.

X. ACKNOWLEDGEMENTS

The authors would like to thank the Blue Water Undergraduate Petascale Education Program and Shodor for their financial and educational support. Furthermore, this work used the Extreme Science and Engineering Discovery Environment (XSEDE), which is supported by National Science Foundation grant number OCI-1053575. I.S. is thankful to the Alexander von Humboldt foundation and acknowledges the support of the High Performance Computer Center and the Institute for Cyber-Enabled Research at Michigan State University. T.S. is grateful for useful conversations with LANL physicists James Cooley and James Mercer-Smith that helped guide his contribution to this work.

- [1] R. K. Agarwal, K.-Y. Yun, and R. Balakrishnan, *Physics of Fluids* **13**, 3061 (2001).
- [2] I. D. Boyd, G. Chen, and G. V. Candler, *Physics of Fluids* **7**, 210 (1995).
- [3] Z.-H. Li and H.-X. Zhang, *Journal of Computational Physics* **228**, 1116 (2009).
- [4] Y. W. Yap and J. E. Sader, *Physics of Fluids* **24**, 032004 (2012).
- [5] J. Aichelin and H. Stöcker, *Physics Letters B* **176**, 14 (1986).
- [6] I. Bouras, E. Molnár, H. Niemi, Z. Xu, A. El, O. Fochler, C. Greiner, and D. H. Rischke, *Phys. Rev. C* **82**, 024910 (2010).
- [7] G. Kortemeyer, W. Bauer, K. Haglin, J. Murray, and S. Pratt, *Phys. Rev. C* **52**, 2714 (1995).
- [8] M. Casanova, O. Larroche, and J.-P. Matte, *Phys. Rev. Lett.* **67**, 2143 (1991).
- [9] F. Vidal, J. P. Matte, M. Casanova, and O. Larroche, *Physics of Fluids B: Plasma Physics* **5**, 3182 (1993).
- [10] F. Vidal, J. P. Matte, M. Casanova, and O. Larroche, *Phys. Rev. E* **52**, 4568 (1995).
- [11] T. Strother and W. Bauer, *International Journal of Modern Physics D* **19**, 1483 (2010).
- [12] J. D. Lindl, P. Amendt, R. L. Berger, S. G. Glendinning, S. H. Glenzer, S. W. Haan, R. L. Kauffman, O. L. Landen, and L. J. Suter, *Physics of Plasmas* **11**, 339 (2004).
- [13] O. Larroche, *European Physical Journal D* **27**, 131 (2003).
- [14] G. A. Bird, *Molecular gas dynamics and the direct simulation of gas flows* (Clarendon Press, 1994).
- [15] J. Struckmeier and K. Steiner, *Physics of Fluids* **7**, 2876 (1995).
- [16] A. Nordsieck and B. L. Hicks, in *Rarefied Gas Dynamics, Volume 1*, edited by C. L. Brundin (1967), p. 695.
- [17] P. A. Amendt, J. L. Milovich, S. C. Wilks, C. K. Li, R. D. Petrasso, and F. H. Sguin, *Plasma Physics and Controlled Fusion* **51**, 124048 (2009).
- [18] P. Amendt, S. C. Wilks, C. Bellei, C. K. Li, and R. D. Petrasso, *Physics of Plasmas* **18**, 056308 (pages 11) (2011).
- [19] S. A. Colgate and R. H. White, *Astrophys. Journal* **143**, 626 (1966).
- [20] H. A. Bethe and J. R. Wilson, *Astrophys. Journal* **295**, 14 (1985).
- [21] A. Burrows, E. Livne, L. Dessart, C. D. Ott, and J. Murphy, *Astrophys. Journal* **640**, 878 (2006).
- [22] G. S. Bisnovatyi-Kogan, *Soviet Astronomy* **14**, 652 (1971).
- [23] J. M. LeBlanc and J. R. Wilson, *Astrophys. Journal* **161**, 541 (1970).
- [24] I. Sagert, T. Fischer, M. Hempel, G. Pagliara, J. Schaffner-Bielich, A. Mezzacappa, F.-K. Thielemann, and M. Liebendörfer, *Physical Review Letters* **102**, 081101 (2009).
- [25] H. Janka, K. Langanke, A. Marek, G. Martínez-Pinedo, and B. Müller, *Physics Reports* **442**, 38 (2007).
- [26] J. M. Blondin, A. Mezzacappa, and C. DeMarino, *Astrophys. Journal* **584**, 971 (2003).
- [27] M. Herant, W. Benz, W. R. Hix, C. L. Fryer, and S. A. Colgate, *Astrophys. Journal* **435**, 339 (1994).
- [28] C. L. Fryer and M. S. Warren, *Astrophys. Journal Letters* **574**, L65 (2002).
- [29] J. Nordhaus, A. Burrows, A. Almgren, and J. Bell, *Astrophys. Journal* **720**, 694 (2010).
- [30] T. Takiwaki, K. Kotake, and Y. Suwa, *Astrophys. Journal* **749**, 98 (2012).
- [31] F. Hanke, A. Marek, B. Müller, and H.-T. Janka, *Astrophys. Journal* **755**, 138 (2012).
- [32] M. Liebendörfer, M. Rampp, H. Janka, and A. Mezzacappa, *Astrophys. Journal* **620**, 840 (2005).
- [33] M. Liebendörfer, O. E. B. Messer, A. Mezzacappa, S. W. Bruenn, C. Y. Cardall, and F. Thielemann, *Astrophys. Journal, Suppl.* **150**, 263 (2004).
- [34] M. Rampp and H. Janka, *Astronomy and Astrophysics* **396**, 361 (2002).
- [35] S. W. Bruenn, A. Mezzacappa, W. R. Hix, J. M. Blondin, P. Marronetti, O. E. B. Messer, C. J. Dirk, and S. Yoshida (2010).
- [36] M. Liebendörfer, S. C. Whitehouse, and T. Fischer, *Astrophys. Journal* **698**, 1174 (2009).
- [37] E. Livne, A. Burrows, R. Walder, I. Lichtenstadt, and T. A. Thompson, *Astrophys. Journal* **609**, 277 (2004).

- [38] A. Marek and H. Janka, *Astrophys. Journal* **694**, 664 (2009).
- [39] Y. Suwa, K. Kotake, T. Takiwaki, S. C. Whitehouse, M. Liebendoerfer, and K. Sato (2009).
- [40] E. Abdikamalov, A. Burrows, C. D. Ott, F. Löffler, E. O'Connor, J. C. Dolence, and E. Schnetter, *Astrophys. Journal* **755**, 111 (2012).
- [41] S. I. Blinnikov, I. V. Panov, M. A. Rudzsky, and K. Sumiyoshi, *Astronomy and Astrophysics* **535**, A37 (2011).
- [42] K. Sumiyoshi, *Nuclear Physics B Proceedings Supplements* **159**, 27 (2006).
- [43] K. Langanke and G. Martínez-Pinedo, *Reviews of Modern Physics* **75**, 819 (2003).
- [44] T. Strother, Ph.D. thesis, Michigan State University, East Lansing, Michigan (2009).
- [45] C. Cercignani and M. Lampis, *Transport Theory Stat. Phys.* **1**, 101114 (1971).
- [46] S. Chapman and T. G. Cowling, *The mathematical theory of non-uniform gases* (Cambridge: University Press, 1970, 3rd ed., 1970).
- [47] J. E. Broadwell, *Journal of Fluid Mechanics* **19**, 401 (1964).
- [48] Z.-H. Li and H.-X. Zhang, *Journal of Computational Physics* **193**, 708 (2004).
- [49] K. Xu and J.-C. Huang, *IMA Journal of Applied Mathematics* (2011).
- [50] S. Liu and C. Zhong, *Phys. Rev. E* **85**, 066705 (2012).
- [51] B. J. Alder and T. E. Wainwright, *The Journal of Chemical Physics* **31**, 459 (1959).
- [52] F. R. Graziani, V. S. Batista, L. X. Benedict, J. I. Castor, H. Chen, S. N. Chen, C. A. Fichtl, J. N. Glosli, P. E. Grabowski, A. T. Graf, et al., *High Energy Density Physics* **8**, 105 (2012).
- [53] K. Kadau, T. C. Germann, and P. S. Lomdahl, *International Journal of Modern Physics C* **17**, 1755 (2006).
- [54] M. S. Murillo and M. W. C. Dharmawardana, *Phys. Rev. Lett.* **100**, 205005 (2008).
- [55] C.-Y. Wong, *Phys. Rev. C* **25**, 1460 (1982).
- [56] G. A. Bird, *Physics of Fluids* **6**, 1518 (1963).
- [57] G. A. Bird, in *Rarefied Gas Dynamics, Volume 1*, edited by J. H. de Leeuw (1965), p. 216.
- [58] G. D. Westfall, W. Bauer, D. Craig, M. Cronqvist, E. Gaultieri, S. Hannuschke, D. Klakow, T. Li, T. Reposeur, A. M. Vander Molen, et al., *Physical Review Letters* **71**, 1986 (1993).
- [59] T. Strother and W. Bauer, *International Journal of Modern Physics E* **16**, 1073 (2007).
- [60] G. A. Bird, *Physics of Fluids* **13**, 2676 (1970).
- [61] G. F. Bertsch, H. Kruse, and S. D. Gupta, *Phys. Rev. C* **29**, 673 (1984).
- [62] S.-J. Wang, B.-A. Li, W. Bauer, and J. Randrup, *Annals of Physics* **209**, 251 (1991).
- [63] W. Bauer and T. Strother, *International Journal of Modern Physics E* **14**, 129 (2005).
- [64] G. Kortemeyer, F. Daffin, and W. Bauer, *Physics Letters B* **374**, 25 (1996).
- [65] S. Sorensen and W.-Q. Chao, *Commun. Theor. Phys.* **21**, 317 (1994).
- [66] G. A. Sod, *Journal of Computational Physics* **27**, 1 (1978).
- [67] W. F. Noh, *Journal of Computational Physics* **72**, 78 (1987).
- [68] Á. Mulero, ed., *Theory and Simulation of Hard-Sphere Fluids and Related Systems*, vol. 753 of *Lecture Notes in Physics*, Berlin Springer Verlag (2008).
- [69] J. H. Irving and J. G. Kirkwood, *J. Chem. Phys.* **18**, 817 (1950).
- [70] E. J. Tasker, R. Brunino, N. L. Mitchell, D. Michelsen, S. Hopton, F. R. Pearce, G. L. Bryan, and T. Theuns, *MNRAS* **390**, 1267 (2008).
- [71] B. Fryxell, K. Olson, P. Ricker, F. X. Timmes, M. Zingale, D. Q. Lamb, P. MacNeice, R. Rosner, J. W. Truran, and H. Tufo, *Astrophys. Journal Suppl.* **131**, 273 (2000).
- [72] N. Crouseilles, P. Degond, and M. Lemou, *Journal of Computational Physics* **199**, 776 (2004).
- [73] Z.-H. Li and H.-X. Zhang, *Journal of Computational Physics* **193**, 708 (2004).
- [74] M. Smith, H. Cave, J.-S. Wu, M. Jermy, and Y.-S. Chen, *Journal of Computational Physics* **228**, 2213 (2009).
- [75] Y. Gan, A. Xu, G. Zhang, X. Yu, and Y. Li, *Physica A: Statistical Mechanics and its Applications* **387**, 1721 (2008).
- [76] K. Xu and J.-C. Huang, *Journal of Computational Physics* **229**, 7747 (2010).
- [77] P. Degond, G. Dimarco, and L. Mieussens, *Journal of Computational Physics* **229**, 4907 (2010).
- [78] B. Fryxell and F. X. Timmes, *Verification Problems*, Arizona State University, Tempe, USA (April 2012).
- [79] F. Chen, A. Xu, G. Zhang, and Y. Li, *Physics Letters A* **375**, 2129 (2011).
- [80] M. Bennoune, M. Lemou, and L. Mieussens, *Journal of Computational Physics* **227**, 3781 (2008).
- [81] J. M. Marti and E. Mueller, *Living Reviews in Relativity* **2** (1999).